Contrib Mineral Petrol (2006) 151: 71–87
DOI 10.1007/s00410-005-0046-3

ORIGINAL PAPER

Yang Liu · Alfred T. Anderson · Colin J. N. Wilson
Andrew M. Davis · Ian M. Steele

Mixing and differentiation in the Oruanui rhyolitic magma, Taupo, New Zealand: evidence from volatiles and trace elements in melt inclusions

Received: 11 March 2005 / Accepted: 25 October 2005 / Published online: 8 December 2005

Abstract Large pyroclastic rhyolites are snapshots of evolving magma bodies, and preserved in their eruptive pyroclasts is a record of evolution up to the time of eruption. Here we focus on the conditions and processes in the Oruanui magma that erupted at 26.5 ka from Taupo Volcano, New Zealand. The 530 km^3 (void-free) of material erupted in the Oruanui event is comparable in size to the Bishop Tuff in California, but differs in that rhyolitic pumice and glass compositions, although variable, did not change systematically with eruption order. We measured the concentrations of H_2O, CO_2 and major and trace elements in zoned phenocrysts and melt inclusions from individual pumice clasts covering the range from early to late erupted units. We also used cathodoluminescence imaging to infer growth histories of quartz phenocrysts. For quartz-hosted inclusions, we studied both fully enclosed melt inclusions and reentrants (connecting to host melt through a small opening). The textures and compositions of inclusions and phenocrysts reflect complex pre-eruptive processes of incomplete assimilation/partial melting, crystallization differentiation, magma mixing and gas saturation. 'Restitic' quartz occurs in seven of eight pumice clasts studied. Variations in dissolved H_2O and CO_2 in quartz-hosted melt inclusions reflect gas saturation in the Oruanui magma and crystallization depths of ~3.5–7 km. Based on variations of dissolved H_2O and CO_2 in reentrants, the amount of exsolved gas at the beginning of eruption increased with depth, corresponding to decreasing density with depth. Pre-eruptive mixing of magma with varying gas content implies variations in magma bulk density that would have driven convective mixing.

Keywords Melt inclusions · Rhyolite · Cathodoluminescence · Magma convection · Oruanui eruption · Quartz

Electronic Supplementary Material Supplementary material is available for this article at http://dx.doi.org/10.1007/s00410-005-0046-3 and is accessible for authorized users.

Communicated by: T. L. Grove

Y. Liu · A. T. Anderson · I. M. Steele
Department of Geophysical Sciences, University of Chicago, 5734 S. Ellis Ave, Chicago, IL, 60637 USA

C. J. N. Wilson
Department of Geology, University of Auckland, Private Bag 92019, Auckland, New Zealand

A. M. Davis
Department of Geophysical Sciences, Enrico Fermi Institute, and Chicago Center for Cosmochemistry, University of Chicago, 5640 S. Ellis Ave, Chicago, IL, 60637 USA

Y. Liu (✉)
Department of Earth and Planetary Sciences, University of Tennessee, Knoxville, TN, 37996 USA
E-mail: yangl@utk.edu
Tel.: +1-865-9740402
Fax: +1-865-9742368

Conceptual background

The evolution of the continental crust requires the formation, crystallization and degassing of silicic magma, where degassing can occur by volcanic eruption or in plutonic settings. The textures and compositions of large pyroclastic rhyolites constrain concepts of magma formation and evolution, and these arguably apply to batholithic additions to continental crust and their degassing. Understanding the origin and evolution of silicic magmas benefits from study, in particular, of individual volcanic pumice clasts and their contained crystals as these comprise the record of magmatic evolution including composition, pressure, temperature, gas content, bulk density and dynamical behavior.

Broadening our understanding from detailed study of individual volcanic rhyolites to general ideas about the formation of continental crust (which is largely composed of silicic plutonic rocks) can be advanced through studies of various 'end-member' types of rhyolites. The

differences between rhyolites and plutonic counterparts are related in part to which rhyolitic magmas are more volatile-rich, or which were unsystematically stratified, or dynamically unstable. Our goal in the present work is to document and thus constrain ideas about one of those pyroclastic rhyolites, for which the relations between stratigraphy (sequence of eruption and deposition), composition and texture are unsystematic.

Chemical and mineralogical compositions and textures of pumice clasts commonly vary in large pyroclastic rhyolites (Smith 1979; Hildreth 1981). In some cases variations are systematic with stratigraphy (e.g., Bandelier Tuff, New Mexico: Smith and Bailey 1966; Bishop Tuff, California: Hildreth 1977, 1979). In the Oruanui case considered here, pumice compositions do not vary systematically with stratigraphy. Our work shows that these unsystematic variations reflect pre-eruptive stirring, probable variations in gas content, and dynamical instability.

Geological setting and history

Taupo volcano is a vigorously active caldera center in the central Taupo Volcanic Zone (TVZ) in North Island, New Zealand (Fig. 1). Activity in the area of Taupo volcano began after ~320 ka (Wilson 1993; unpublished data). From ~320 to ~150 ka numerous relatively small-scale pyroclastic and lava-forming eruptions occurred, with compositional variations that define several broad geographical and temporal groups (Sutton et al. 1995). During this time period, Maroa volcano immediately to the north of Taupo was much more frequently active. From ~150 ka onwards, the main focus of activity moved south from Maroa into the area just north of Lake Taupo, generating several domes and dome complexes. Of these, the Whakaroa domes (Fig. 1) have broadly similar chemistries to the later Oruanui eruptives, with overlap in $^{87}Sr/^{86}Sr$ ratios, but are markedly more crystal-rich, and some have biotite (Sutton et al. 1995). From ~65 to 26.5 ka, rhyolites of similar chemical and isotopic characteristics to that of the Oruanui rhyolites erupted in at least 3 events at ~65, ~45 and 29 ka, interspersed with rhyolites of contrasting mineralogy and composition that discharged nearby at Ngangiho (~45 ka) and at the Trig 9471 and Rubbish Tip domes at ~27.3 ka (Fig. 1; Sutton et al. 1995; Wilson et al. 2002, 2005). Occurring at 26.5 ka, the Oruanui eruption was by far the largest event at Taupo volcano, discharging ~530 km^3 of void-free magma that is mostly rhyolitic and produced the shape of the volcano in its present day form (Wilson 2001; Wilson et al. 2005). Compositions of post-Oruanui Taupo rhyolite pumices and lavas show distinctly different major element and isotope characteristics from Oruanui rhyolites (Sutton et al. 1995, 2000), with no evidence for involvement of the earlier eruptives in any mixing trend. However, Arculus et al. (2005) reported compositions of melt inclusions hosted in plagioclase, pyroxene and Fe–Ti oxide crystals in the post-Oruanui rhyolites that overlapped with the compositions of the Oruanui rhyolites, possibly reflecting some magma mingling/mixing.

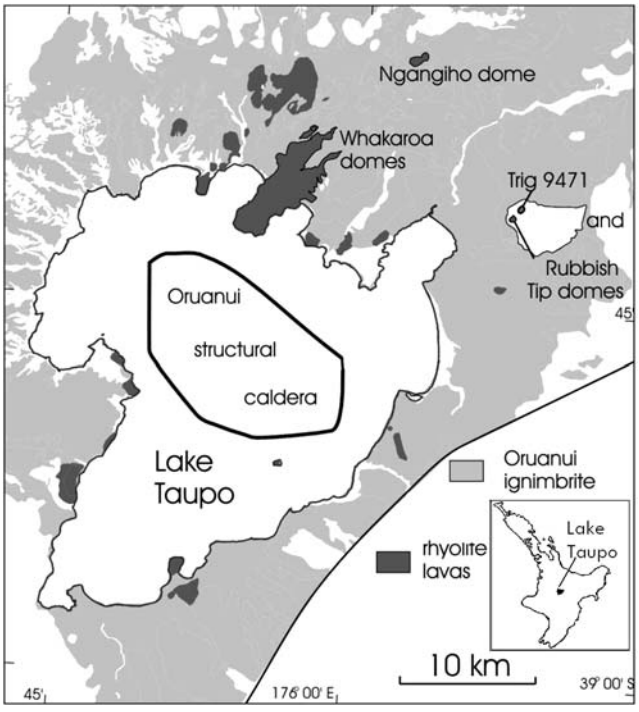

Fig. 1 Simplified map of Taupo Volcano and surrounding area. Areas in *dark gray* are rhyolitic lava and those in *light gray* represent the Oruanui ignimbrite. The named domes north of Lake Taupo were active in the ~65–26.5 ka build-up to the Oruanui eruption (see Wilson et al. 2005). *Inset* is the location map for Taupo volcano in the North Island of New Zealand

Sample characterization and petrography

We studied eight individual Oruanui pumice clasts sampled from 'early' (four from phase 1 and one from phase 2), 'middle' (one from phase 9) and 'late' (two from phase 10) deposits of the Oruanui eruption (Wilson 2001) (Table 1). Clast densities, and crystal and vesicle contents show no correlation with eruptive order (Table 1). Crystal contents are between 6 and 13 wt%, which is similar to other Oruanui pumice clasts in Wilson et al. (2005). The relative abundances of major phenocrysts in several clasts are roughly 70–75 wt% plagioclase, 10–15 wt% quartz, 5–10 wt% orthopyroxene, and 1–2 wt% amphibole, similar to the values reported for the dominant Oruanui rhyolite by Wilson et al. (2005). The abundances of magnetite and ilmenite are generally < 1 wt% of phenocrysts. In all clasts, most of the volume of plagioclase occurs as phenocrysts < 2 mm across. Quartz crystals larger than 0.8 mm are commonly fractured with glass-free surfaces, which are inferred to result from the sample preparation process. All orthopyroxene phenocrysts larger than ~200 μm contain many melt and mineral inclusions (of apatite,

Table 1 Density, phenocryst content, and vesicularity of pumice clasts

Sample	Density (kg m^{-3})	Crystal content (wt%)	Vesicularity [a] (vol%)	Stratigraphic position [b]
Late				
P1537	605	8	74	Uppermost preserved ignimbrite
P1541/T1[c]	ND	10	ND	Same as above
P1541/T3[c]	ND	10	ND	Same as above
Middle				
P1508[d]	764	8	67	Top of unit 9
Early				
P1408	572	7	75	Ignimbrite interbedded with Fall unit 2
P1577	725	10	69	Topmost 10–30 cm from top of Fall unit 1 where 223 cm thick
P1412	595	6	74	Middle (38–46 cm above base) of Fall unit 1 where 108 cm thick
P1573	703	13	70	10–15 cm above base of Fall unit 1 where 223 cm thick
P1573/W1[c]	ND	8	ND	Same as above
P1573/W2[c]	ND	8	ND	Same as above

All pumice clasts are white in color and have similar vesicle sizes from edge to center

[a] Vesicularity of the pumice was calculated using 2,300 kg m^{-3} for glass and 2,800 kg m^{-3} for bulk crystals. Vesicles are elongate in sample P1508 and P1541, but are nearly spherical in other samples. ND indicates not determined

[b] Stratigraphic positions are from Wilson (2001)

[c] Sample P1541/T1 and P1541/T3 are from the same clast. Sample P1573/W1 and P1573/W2 are from the same clast.

[d] Sample 1508 has 'porphyroclastic' texture where a few large round plagioclase crystals (< 1 vol%) up to 8 mm diameter are embedded in the glass

ilmenite, and magnetite). Some magnetite grains contain round zircon inclusions. Most Fe–Ti oxide inclusions in amphibole are ilmenite. Some pumice clasts contain < 1 vol% intergrown crystal clots (of orthopyroxene, amphibole, and quartz) a few mm in diameter.

Sample preparation and analytical methods

In order to obtain magma compositions, we studied individual pumice clasts of several centimeters in diameter. Prior to determination of its density and crystal content, each clast was dried in an oven at ~90°C and cleaned to remove adhering crystals and pumice fragments. We crushed and separated crystals using the same procedure as Skirius et al. (1990) and Wallace et al. (1999). Crystals from several clasts (P1408, P1508, P1573) were separated using heavy liquids. Quartz grains with uncracked melt inclusions were hand-picked from refractive index liquids and then sectioned and polished. For analysis of volatile contents, quartz crystals larger than 0.5 mm were doubly polished to a thickness of 40–273 μm to expose melt inclusions on two near-parallel surfaces. We used the method of Skirius et al. (1990) to determine the thickness of the inclusion: the quartz wafer was attached to a spindle stage and submerged in reference index liquid ($n = 1.54$). Precautions were taken to assure a flat (non-distorting) and stable surface above the crystal and spindle. The thickness of the inclusion was then measured using a Zeiss Universal petrographic microscope with a graduated ocular calibrated with a stage micrometer. Uncertainties in the thickness measurements are mostly < 5 μm.

Concentrations of dissolved H_2O and CO_2 in quartz-hosted melt inclusions (Table 2) were determined by Fourier transform infrared (FTIR) spectroscopy using a microscope attached to a Perkin-Elmer GX FTIR spectrometer at the University of Michigan. Analytical conditions include a visible source, a CaF_2 beamsplitter, a liquid-N_2-cooled MCT detector, and a square aperture (width and length of 20–50 μm). We used the calibration of Zhang et al. (1997) for H_2O species and an absorption coefficient of 1,214 l cm^{-1} mol^{-1} for CO_2 (Behrens et al. 2004). Uncertainties (1σ) of the analysis include errors in measuring sample thicknesses and FTIR-peak intensities, and are typically ≤ 0.3 wt% for H_2O and ≤ 10 ppm for CO_2. Occasional larger uncertainties in volatile contents are caused by variations in thickness across some wafers and the poor quality of some FTIR spectra.

Cathodoluminescence (CL) images (Fig. 2 and Appendix A, deposited as electronic data) were collected from the same wafers used for FTIR analysis using a photomultiplier attached to a Cameca SX-50 electron microprobe at the University of Chicago. Analytical conditions were similar to those of Peppard et al. (2001). All images are 256×256 pixels and were obtained at 15 kV with a 50 nA current.

Major-element compositions of melt inclusions in quartz, plagioclase, pyroxene and magnetite (Appendix B, electronic data) were determined using the Cameca SX-50 electron microprobe with a defocused beam (diameter of ~10 μm), 15 kV voltage, and 10 nA current. To minimize alkali loss, Na and K were analyzed first with a short collection time (10 s). Electron probe analyses were conducted before collecting CL images.

Analyses of 27 trace elements in melt inclusions were performed on a modified AEI IM-20 ion microprobe at the University of Chicago using the revised procedures of MacPherson and Davis (1994). Uncertainties of

Table 2 FTIR spectroscopic data for H_2O and CO_2 in Oruanui melt inclusions in quartz.

Inclusions [a]	A_{5200}(mm^{-1})	A_{4500}(mm^{-1})	A_{2350}(mm^{-1})	H_2O_t(wt%)	CO_2(ppm)	P_{sat} (MPa)	Comments[b]
P1537							
1-2[e]	*0.886*	*0.223*	*0.469*	*4.72*	*74*	*140.4*	
1-3-1	0.818	0.229	1.208	4.48	191	150.2	
1-6-4	0.819	0.207	1.160	4.36	183	143.0	
2-4-2	0.844	0.213	1.134	4.50	184	149.9	1 bb
2-6	0.931	0.264	1.022	5.19 (0.8)	162	181.4	
2-8	0.854	0.211	1.163	4.52	184	150.9	
2-12	0.913	0.206	1.251	4.75 (0.38)	198 (13)	165.0	
2-13	0.868[c]	0.223[c]	1.241[c]	4.65	196 (17)	159.6	
2-16	0.843	0.193	1.006	4.39 (0.39)	159	140.0	
1-12-RE	1.029	0.163	0.066	5.05	10	145.0	1 bb
2-8-RE	0.233	0.199	0.077	1.94	12	27.3	
2-11-RE	0.309	0.182	0.729	2.14	114	48.5	
2-13-RE	0.461	0.181	0.580	2.79	91	64.1	
2-14-RE	0.491	0.172	0.542	2.83	85	64.4	
P1541/T1							
1-6-b	0.900	0.228	1.919	4.81	301	187.6	
1-6-a	0.878	0.176	1.091	4.46	172	145.8	
1-10	0.848	0.191	1.686	4.41	266	160.6	
1-5-RE	0.901	0.204	0.130	4.69	21 (14)	129.1	
P1541/T3							
1-12[e]	*0.835*	*0.192*	*0.483*	*4.35*	*76*	*123.1*	*Part of inclusion was lost*
2-2-2	0.921	0.227	1.244	4.89	197	172.1	
2-3	0.875	0.206	0.549	4.59	87	136.5	1 xtl
2-4	0.836	0.209	1.038	4.44	164	143.4	
2-5-1	0.838	0.206	0.922	4.43	146	139.6	
2-6	0.831	0.185	1.210	4.30	191	141.6	
1-16RE	0.899	0.252	1.362	4.93	216	177.3	
2-1-HG	0.849	0.203	1.225	4.47	193	150.1	
P1508							
1-4	0.854	0.212	0.862	4.53 (0.35)	136 (12)	142.6	1 bb or 1 xtl
1-5[e]	*0.819*	*0.197*	*0.169*	*4.31 (0.4)*	*27*	*112.5*	
2-1	0.851	0.202	0.527	4.47	83	130.0	
2-3	0.818	0.193	0.757	4.29	119	128.1	
2-4	0.872	0.203	0.702	4.56	111	139.4	
2-7-2	0.829	0.192	0.655	4.33	103	127.1	
1-3-RE1	0.613	0.222	0.484	3.59 (0.49)	76	90.5	
1-3-RE2	0.668	0.203	0.470	3.68	74	93.8	
1-4RE	0.792	0.209	0.265	4.27	42	113.4	
1-13RE	0.827	0.205	0.540	4.38	85	126.1	1 bb
1-13HG	0.809	0.199	0.575	4.27	91	122.1	
2-9RE	0.750	0.207	0.180	4.07	28	102.0	
P1408							
1-1	0.733	0.257	0.416	4.27	66	118.1	
1-2	0.790	0.285	0.554	4.67 (0.37)	88	140.5	
1-3[e]	*0.778*	*0.279*	*0.444*	*4.59*	*70*	*133.3*	
1-4	0.737	0.292	0.609	4.5	96	133.8	
1-6	0.752	0.260	0.579	4.37	91	126.8	
1-8	0.800	0.274	0.650	4.64 (0.63)	103 (12)	141.9	
2-1	0.796	0.225	0.511	4.35	81	124.0	
2-2	0.779	0.261	0.505	4.48	80	129.9	1 xtl
2-3	0.760	0.249	0.537	4.34	85	124.3	
2-5	0.790	0.266	0.564	4.56	89	135.4	
1-6-RE	0.788	0.265	0.494	4.54	78	132.4	
1-11-RE	0.411	0.221	0.130	2.77	20	51.9	
2-8-RE	0.441	0.230	0.120	2.94 (0.5)	19	57.2	
2-11-RE	0.600	0.268	0.241	3.81	38	92.8	
P1577							
1-2-1	0.659	0.270	0.777	4.05	122	117.8	
1-5	0.733	0.294	0.471	4.50	74	129.8	
1-13	0.752	0.295	0.410	4.58	65	131.9	
2-1	0.752	0.317	0.282	4.72	45	135.0	
2-7	0.743	0.277	0.437	4.43	69	125.6	
2-2	0.722	0.306	0.368	4.53	58	128.3	3 bb
1-10-RE	0.587	0.318	0.368	4.07 (0.68)	58	107.3	
1-15-RE	0.720	0.278	0.474	4.35	75	122.9	

Table 2 (Contd.)

Inclusions [a]	A_{5200}(mm^{-1})	A_{4500}(mm^{-1})	A_{2350}(mm^{-1})	H_2O_t(wt%)	CO_2(ppm)	P_{sat} (MPa)	Comments[b]
2-16-RE	0.653	0.287	0.329	4.13	52	108.9	
2-17-RE	0.765	0.283	0.409	4.56	65	131.0	
2-19-RE	0.585	0.305	0.090	3.98	14	95.7	
P1412							
1-3	0.640	0.264	0.649	3.94	102	109.5	3 bb
1-8-1	0.617[c]	0.257[c]	0.281[c]	3.81	44	93.9	
1-12	0.693	0.277	0.540	4.23	85	119.3	1 bb
2-7	0.739	0.270	0.489	4.37	77	124.2	
2-16	0.690	0.258	0.435	4.10	69	110.6	
2-20	0.670	0.287	0.964	4.20	152	129.9	
2-23-1	0.686	0.275	0.964	4.19	152	129.4	
2-23-2	0.820	0.331	0.506	5.07 (0.73)	80 (15)	159.3	5 bb
2-25	0.706	0.312	0.858	4.50	136	141.1	
2-26	0.799	0.319	0.637	4.91	101	155.0	1 bb
2-27i	0.747	0.290	0.490	4.52 (0.67)	77	131.2	
2-28	0.670	0.362	0.473	4.30	79	121.4	
2-29	0.659	0.242	0.540	3.89 (0.34)	85	104.4	
2-30	0.763	0.282	0.519	4.54	82	133.1	
2-27-RE	0.670	0.362	0.473	4.69 (0.79)	75	139.1	
P1573							
1-2-1	0.738	0.307	0.813	4.60	129	145.0	
1-2-2	0.711	0.313	0.781	4.53	123	140.4	
1-3	0.718[c]	0.278[c]	0.480[c]	4.34	76	122.7	
1-5	0.684	0.374	0.217	4.84	34	138.9	
1-7-1	0.767	0.328	0.373	4.84	59	144.1	
1-7-2	0.735	0.285	0.171	4.45	27	118.9	
2-1	0.701	0.277	0.505	4.26	80	119.7	
2-3	0.759	0.301	0.671	4.64	106	142.4	2 bb +1 xtl
1-4-RE [d]	0.505	0.268	u.d.	3.43	<10	71.4	
1-10-RE	0.640	0.301	0.284	4.17	45	109.4	
2-13-RE	0.588	0.314	0.223	4.05	35	102.4	
2-17-RE.h	0.623	0.291	0.290	4.04	46	103.9	Head
2-17-RE.n	0.538	0.319	0.184	3.89	29	94.6	Neck
2-19-HG	0.730	0.287	0.626	4.44	99	132.9	
P1573/W1							
2-11	0.709	0.292	0.461	4.38	73	124.0	
P1573/W2							
1-1-1	0.771	0.319	0.293	4.80	46	139.2	
1-1-2	0.789	0.303	0.704	4.77	111	149.8	
1-3	0.769	0.364	0.969	5.21	154	181.0	
1-4-1	0.755	0.303	0.944	4.64	149	150.4	
1-4-2	0.782	0.313	0.995	4.81	157	160.4	
1-2-RE	0.962	0.183	0.253	4.85	40	140.5	

[a] Melt inclusions are grouped by individual pumice clasts. Inclusions are identified as *X*-*Y*(-*Z*), where *X* refers to crystal size bin (1 for >0.8 mm and 2 for 0.5–0.8 mm), *Y* to crystal number, and *Z* to inclusion number or type. *Z* is not shown if only one melt inclusion was studied. RE indicates reentrant and HG is reentrant with a thin tube (hourglass). Concentration of the total dissolved H_2O (H_2O_t) was calculated using the calibration of Zhang et al. (1997) for H_2O species. The calibration (1,214 l mol^{-1} cm^{-1}) of Behrens et al. (2004) was used to calculate the dissolved CO_2 contents. Uncertainties (1σ) are based on errors of sample thickness and FTIR peak intensity and are generally < 0.3 wt% for H_2O_t and 10 ppm for CO_2 unless otherwise specified. Large uncertainties are caused by the poor quality of some FTIR spectra and/or large error in some thickness measurements. Saturation pressure (P_{sat}) was calculated at 760 °C using the empirical model of Liu et al. (2005)

[b] bb indicates bubbles and xtl are mineral entrapped

[c] FTIR analyses may include a small amount of quartz. The exact amount cannot be calculated but is estimated to be small ($<1\%$)

[d] CO_2 in the reentrant is below detection limit of FTIR ($\sim$ 10 ppm)

[e] Melt inclusions located in jagged CL cores

analysis (2σ) based on counting statistics are small (Appendix C, electronic data). Replicate analyses of five inclusions from Wallace et al. (1999) are within error of earlier results for Mn, Sr, Ba, Pr, Nd, Sm, and Pb, but for other elements the differences (e.g., $\sim$15% for Rb, $\sim$17% for Nb, 6% for Zr, and 13% for La) are larger than analytical uncertainty. Five years elapsed between these two analytical sessions and all analyses in this study were conducted over 2 months. Therefore, we use only the counting statistics as the uncertainty for each element. Concentrations of 13 trace elements in the quartz host crystals also were obtained under the same analytical conditions (Appendix C). To avoid contamination from melt inclusions, either the quartz was ana-

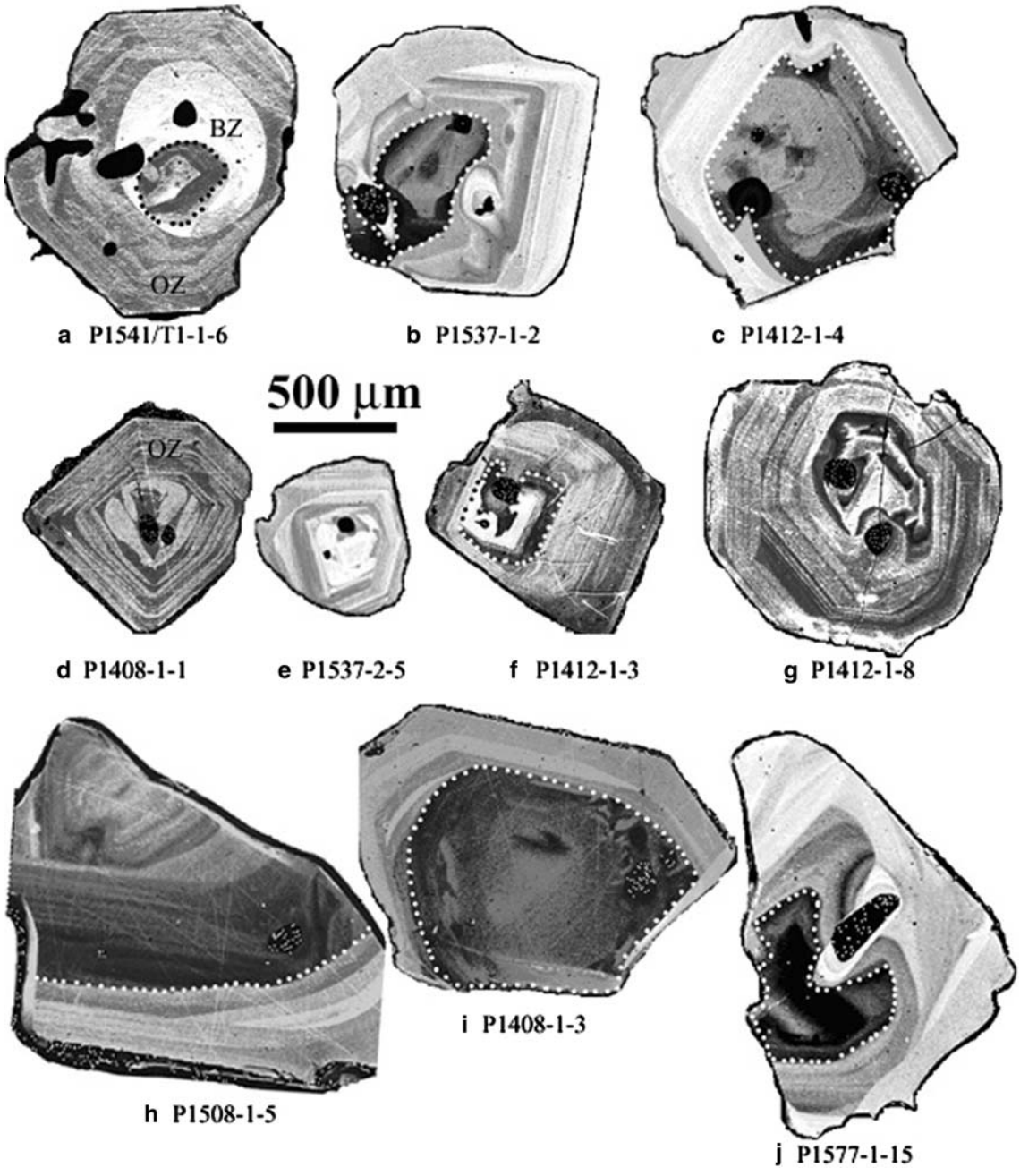

Fig. 2 CL images of selected quartz wafers. All images were adjusted so that they have the same scale (the *scale bar* is 500 μm). The jagged CL cores mantled by dark CL zones in (*a–c*), (*f*), and (*h–i*) are delineated by *dotted curves*. Most melt inclusions appear black with white speckles (noise) and are visible in all crystals. Inclusion in (*f*) was formed later than the *dark zone* surrounding the *white core* and thus is not in the jagged core. Inclusion in (*i*) is a reentrant and is not in the jagged core. Bright zone (*BZ*) in (*a*) refers to the round white zone and OZ in (*a*) and (*d*) marks the oscillatory zoned region

lyzed before melt inclusions or its surface was 'cleaned' using a rastered beam before analysis.

CL zoning in melt-inclusion-bearing quartz

We collected CL images of 80 quartz grains >0.5 mm in diameter: 44 grains from early, 11 grains from middle, and 25 grains from late erupted pumice clasts (Appendix A). The patterns of CL zoning vary widely between the quartz crystals in individual pumice clasts and include four distinct textures:

1. Ubiquitous *oscillatory zoning* (e.g., Fig. 2a, d [labeled OZ], f, g) is marked by numerous zones of alternating moderately brighter and duller CL that are parallel to each other and the external crystal faces (often found

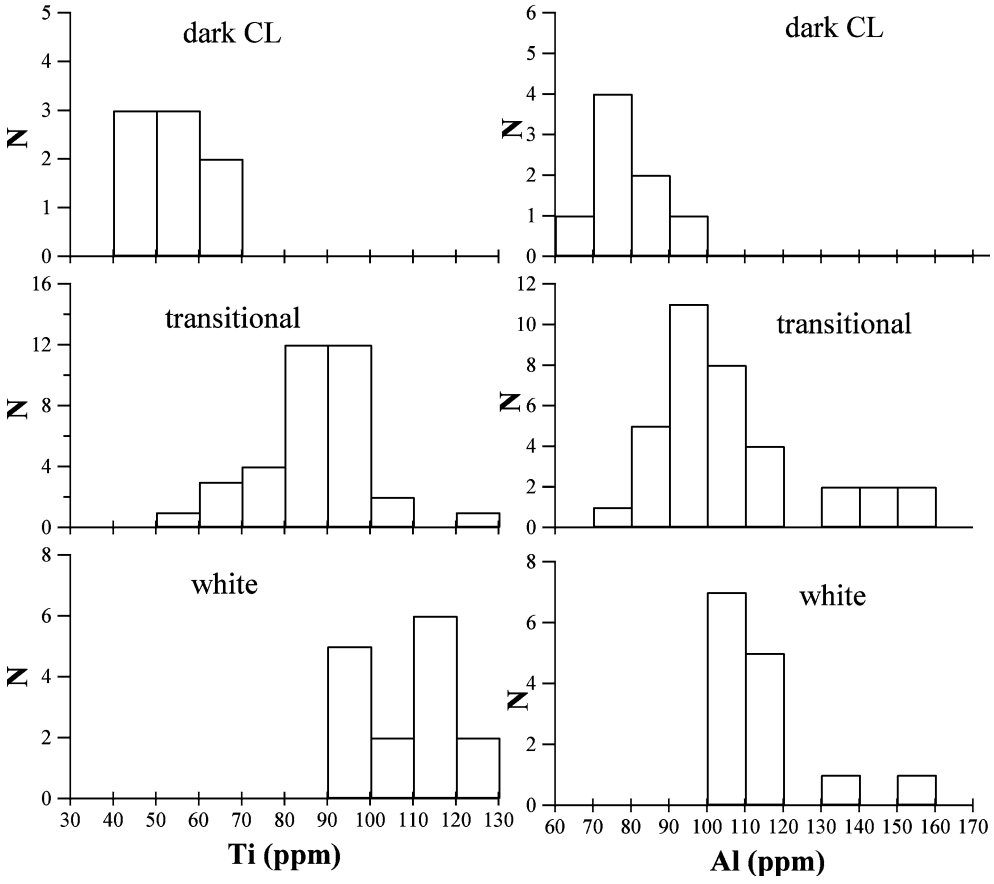

Fig. 3 Al and Ti contents in quartz with different CL intensities. Dark CL refers to analyses on the dark CL zone surrounding the jagged CL cores. Transitional CL refers to quartz with CL intensity ranging between *dark* and *white* or the beam spot was on the oscillatory zones

in quartz from extrusive rocks: Götze et al. 2001). These oscillatory zones are most common just inside the crystal rim but also occur near some crystal centers (close to the 3-D dimensional geometrical center). Most individual oscillatory zones are thinner than ~35 μm.

2. Some crystals (~13 grains) have *irregular core zones* that have bright CL (Fig. 2e–g). Some of these are skeletal (Fig. 2g).
3. Several crystals (~10 grains) have *wide bright CL zones* (Fig. 2a [labeled BZ], b, c, f), which are commonly free of melt inclusions. Most of these are >100 μm wide and at least partly discordant (Fig. 2a, b, f). Wide bright zones occur both in the crystal interior (Fig. 2a) and near the rim (Fig. 2b, c). Some may be rounded (Fig. 2a), but most are flat and parallel to crystal faces (Fig. 2b, c).
4. Some crystals (~10 grains) have *jagged core zones* surrounded by a darker zone that fills in the jagged shape yielding a smoother perimeter (delineated with dotted curves in Fig. 2a–c f, h–j). The jagged cores also have moderately bright CL and oscillatory zoning. Quartz with jagged cores occurs in all but one of the eight pumice clasts. Ti and Al contents in the dark CL quartz surrounding the jagged core are lower than those in bright CL quartz (Fig. 3).

Low Ti content in the dark CL quartz possibly reflects a lower formation temperature or a lower activity of Ti in the melt (Wark and Watson 2004) whereas the jagged boundary of the core plausibly suggests a partial melting event. Therefore, the jagged CL cores are plausibly residues from incomplete melting or partial assimilation of xenocrysts and antecrysts (crystals from previously intruded rocks, see Charlier et al. 2005). Jagged cores are associated with some compositionally anomalous melt inclusions (see below).

There is no correlation of CL zoning patterns with eruptive sequence. Jagged cores occur mainly in large crystals. Grains with crystal faces commonly contain oscillatory zones conformable to the face, while grains with irregular surfaces contain discordant bright to moderately bright zones.

Textures of quartz-hosted melt inclusions

In each pumice clast, there are two types of melt inclusions: fully enclosed inclusions (Fig. 4a) and reentrants (Fig. 4b, c). Reentrants are melt inclusions connecting to matrix glass through a tube, of which those with a very thin tube are termed hourglasses (Fig. 4c). Owing to their open nature, compositions of reentrant and hour-

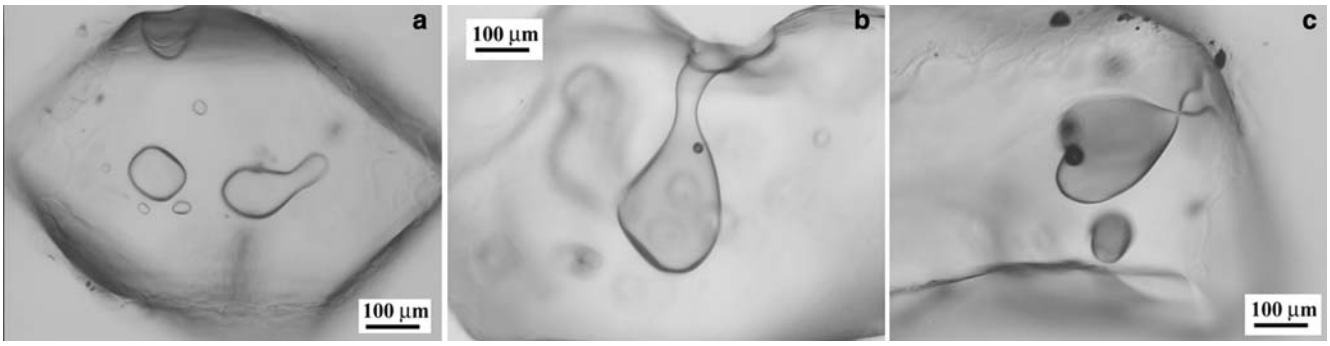

Fig. 4 Types of melt inclusions in Oruanui quartz crystals. **a** Fully enclosed melt inclusions in quartz crystal P1573-2-1 have irregular to round shapes. **b** The reentrant in quartz crystal P1508-1-13 with a bubble attached to the wall. **c** Special type (hourglass) of reentrant with a thin tube in quartz crystal P1541/T3-2-8 with two bubbles attached to the wall. All crystals are viewed in oil with a refraction index of 1.494, close to that of the rhyolitic glass, which adheres to the crystals and contains some enclosed, unconnected bubbles especially visible in **c**

glass inclusions reflect melt compositions and magma chamber conditions at a point closer to the time of eruption than the fully enclosed melt inclusions. This unique feature of reentrants and hourglasses is used in the discussion to estimate pre-eruptive gas content in the magma. In the following discussion, 'melt inclusions' refers to only fully enclosed inclusions and 'reentrants' to open inclusions. Melt inclusions analyzed are from all of the various CL zones described above, and both irregular- and round-shaped melt inclusions can be present in individual crystals (e.g., Fig. 4a). All melt inclusions and reentrants are free of quench crystals but some contain trapped minerals and a few inclusions contain bubbles. The bubble-poor glassy nature of the inclusions suggests that the samples were rapidly quenched, consistent with the inferred phreatomagmatic nature of the Oruanui eruption (Wilson 2001).

Compositions of quartz-hosted melt inclusions and reentrants

All quartz-hosted melt inclusions are weakly peraluminous high-silica rhyolite (Appendix B), similar to the dominant Oruanui pumice compositions (Wilson et al. 2005). Compositions of melt inclusions may be influenced by a chemical boundary layer that is enriched in incompatible elements including volatiles but is depleted in compatible elements (Bacon 1989). If boundary layer effects were important, smaller melt inclusions would be preferentially affected. We infer that the boundary layer effect is insignificant for this study because all melt inclusions analyzed are larger than 50 μm and their trace element contents show no correlation with inclusion size (Appendix C and see Lu et al. 1995). Furthermore, melt inclusions in different host minerals have similar compositions (Appendix B). Below, we first discuss volatile and trace-element contents in non-jagged-core melt inclusions and reentrants and then those within the jagged cores.

H_2O and CO_2 contents in quartz-hosted melt inclusions and reentrants

Ninety-nine melt inclusions and reentrants were analyzed for volatile contents (Table 2, Fig. 5, 6). Dissolved H_2O contents in Oruanui melt inclusions range from 3.8 to 5.2 wt% with an average of ~4.5 wt% (Fig. 5a). FTIR-determined H_2O concentrations are similar to ion-probe-determined concentrations in pyroxene-hosted melt inclusions from the 1.8 ka Taupo plinian fall deposit (Hervig et al. 1989) and in plagioclase- and quartz-hosted inclusions from other pre- and post-Oruanui deposits at Taupo (3.9–6.1 wt%, Dunbar et al. 1989). Most late-erupted Oruanui melt inclusions have higher CO_2 contents (>150 ppm) and gas-saturation pressures (>140 MPa) than early- and middle-erupted melt inclusions (Table 2; Fig. 5a).

If a magma is saturated with gas, then magma crystallizing at greater pressure will contain more H_2O and/or CO_2, as established for equilibrium pressure-dependent H_2O and CO_2 solubility. If magma is not gas-saturated, then it may dissolve more or less H_2O and CO_2 regardless of its pressure. During an eruption, magma that is stored nearest the surface and is thus at the lowest pressure is generally thought to erupt first (Smith and Bailey 1966). A test of gas saturation is that later erupted inclusions should contain greater dissolved H_2O and CO_2 and have greater gas-saturation pressures. Furthermore, the range in gas-saturation pressures computed for various parts of the magma should be consistent with other evidence regarding the depth and thickness of the erupted body of magma (e.g., extent of caldera subsidence).

For the Oruanui magma higher volatile contents and saturation pressures do indeed typify late-erupted clasts (plausibly derived from greater depth). Also the range of gas saturation pressures corresponds to a reasonable thickness of erupted magma. The total range of gas-saturation pressure (94–188 MPa from Table 2) corresponds to a ~3.5 km thick magma layer, which is closely

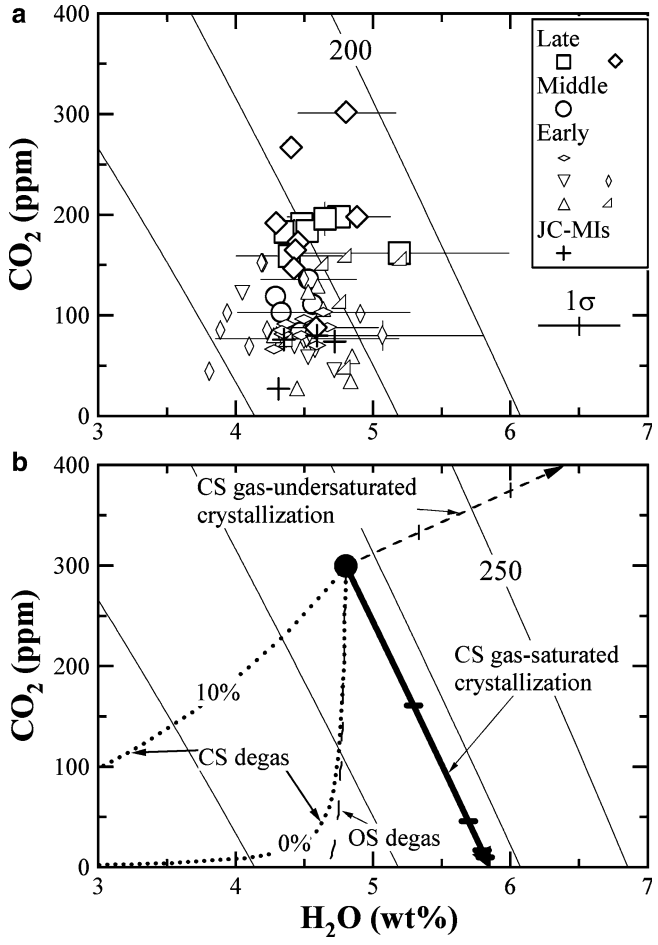

Fig. 5 **a** Dissolved H_2O and CO_2 in Oruanui quartz-hosted melt inclusions. *Different symbol shapes* represent different clasts. Plus signs are melt inclusions in the jagged CL cores (JC-MIs). *Error bars* (1σ) are plotted on lower right hand side. Analyses with uncertainties larger than 1σ are shown individually. **b** Variations of dissolved H_2O and CO_2 in melt for different processes at 760°C, which is the Fe–Ti oxide temperature for the evolved Oruanui rhyolites from Wilson et al. (2005). The solubility model of Liu et al. (2005) is used. *Thin solid curves* are isobars (numbers on curves are pressures in MPa). The *long dashed curve* is the open-system decompression degassing trend (OS degas), while the *short dashed line* represents closed-system gas-undersaturated crystallization. The *thick solid curve* is the trend formed by closed-system gas-saturated crystallization and tick marks are 10% crystallization intervals. *Dotted curves* are closed-system decompression degassing trends (CS degas) with different initial exsolved gas contents (in wt%)

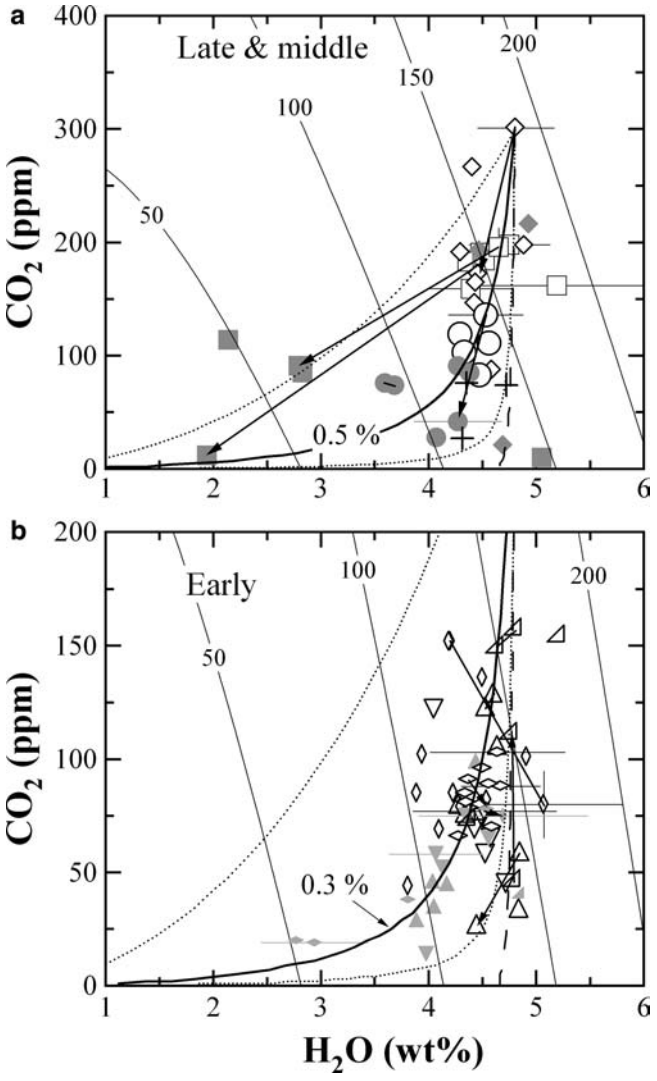

Fig. 6 Dissolved H_2O and CO_2 contents in Oruanui quartz-hosted melt inclusions and reentrants. *Different symbol shapes* correspond to different clasts (as in Fig. 5). *Open symbols* are melt inclusions and corresponding *gray solid symbols* are reentrants in the same clast. Tie lines connect melt inclusions in the same crystal with the *arrow* pointing to the inclusion closer to the edge. *Thin solid curves*, *dotted curves* and *long-dashed curves* are the same as in Fig. 5b. *Thick solid curves* are closed-system decompression degassing trends with 0.5 and 0.3 wt% initially exsolved gas. Note the different *y*-axis scales for CO_2

comparable to the estimate from the magma volume (~530 km^3) and the area of the caldera's structural core (140 km^2, Davy and Caldwell 1998; Wilson 2001). Therefore we infer that crystallization and melt entrapment occurred under gas-saturated conditions. This test of gas saturation in the magma is independent of assumptions of any particular mechanism for the compositional variations. Using the lowest saturation pressure from early-erupted melt inclusions of ~94 MPa (Table 2) and assuming a mean crustal density of 2,670 kg m^{-3} (Davy and Caldwell 1998), the depth of the roof of Oruanui magma body was ~3.5 km below the surface.

All reentrants prepared for FTIR analysis are longer than 90 μm and the innermost regions of reentrants were analyzed. Post-depositional diffusive modifications of H_2O and CO_2 contents in the interior of reentrants are inferred to be small, for two reasons. First, diffusive losses of H_2O and CO_2 during cooling are expected to be small, because the pumice clasts were rapidly quenched (Wilson 2001). Second, diffusive addition of meteoric water to the interior of reentrants has evidently been ineffective as there is less H_2O in reentrants than melt inclusions. At surface temperature, concentration gra-

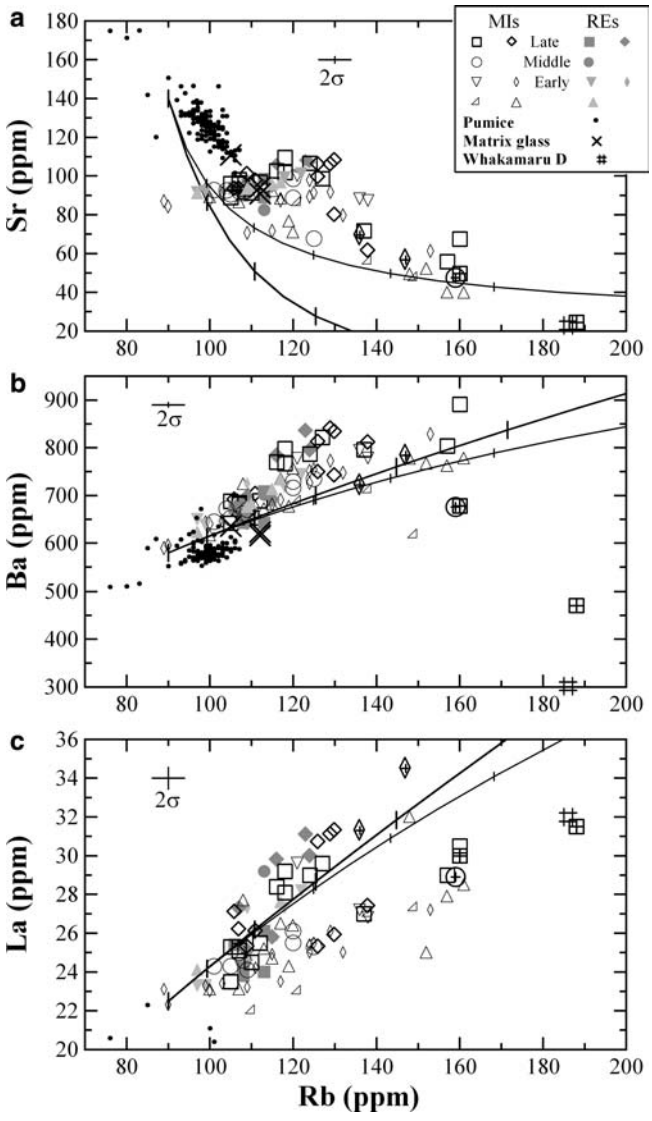

Fig. 7 Variations of selected trace elements in quartz-hosted melt inclusions (*MIs*) and reentrants (*REs*), pumice (*small dots*) and matrix glasses (*crosses*). The glass composition of Whakamaru type D pumice (#) is from Brown et al. (1998). For melt inclusions, different symbol shapes stand for different pumice clasts. Symbols with a plus sign in the center are melt inclusions in the jagged CL cores (JC-MIs), but note that they come from different pumice clasts. *Thick solid curves* are fractional crystallization trends and *thin solid curves* for equilibrium ones, which are calculated using bulk distribution coefficients: $D_{Rb} = 0.07$, $D_{Sr} = 5.54$, $D_{Ba} = 0.47$ $D_{La} = 0.32$ for the Oruanui phenocryst assemblages (72 wt% plagioclase, 16 wt% quartz, 10 wt% orthopyroxene and 2 wt% amphibole). Tick marks are 10% crystallization intervals. Relevant D_s for computation are: for plagioclase (An_{34}), $D_{Rb} = 0.09 \pm 0.01$, $D_{Sr} = 6.8 \pm 0.5$, $D_{Ba} = 0.63 \pm 0.01$, and $D_{La} = 0.32 \pm 0.01$; for quartz are 0; for pyroxene ($En_{66}Wo_4$), $D_{Rb} = 0.039 \pm 0.006$, $D_{Sr} = 6.3 \pm 1.0$, $D_{Ba} = 0.11 \pm 0.03$, and $D_{La} = 0.72 \pm 0.01$; for amphibole, $D_{Rb} = 0.021 \pm 0.006$, $D_{Sr} = 0.77 \pm 0.03$, $D_{Ba} = 0.28 \pm 0.04$, and $D_{La} \approx 0.8$. Partition coefficients of these elements for quartz are assumed to be zero. Partition coefficients of these elements for plagioclase and that of La for orthopyroxene are from Nash and Crecraft (1985) and those of Rb, Sr, and Ba for orthopyroxene and amphibole are from Ewart and Griffin (1994). The partition coefficient of La for amphibole and high silica rhyolite is not well defined and is taken as 0.8 from the GERM database (http://earthref.org/GERM). Uncertainty (2σ) of ion-probe analyses is based on counting statistics. Data for Oruanui pumices and matrix glasses are XRF analyses from Wilson et al. (2005). The uncertainty (2σ) for XRF data (in relative percentage) is 1.5% for Sr and Rb, 3.5% for Ba, and 5% for La.

dients for H_2O are predicted to be <3 μm wide over 26,500 years, since diffusivities of H_2O are so small ($\sim 2\times10^{-12}$ μm^2 s^{-1} at 25°C extrapolated from Zhang and Behrens 2000). In addition, the higher CO_2 content in hourglass inclusions compared to reentrants is interpreted to be a result of lesser fluxes of volatiles through the narrow neck of the hourglass inclusions (Anderson 1991). Volatile contents of most reentrants plausibly evolved during slow ascent of magma and thus roughly follow the trends defined by closed-system decompression and reveal highly variable initial gas contents of 0.3–10 wt% (Fig. 6), an observation that has significant bearing on the pre-eruptive magma bulk density, as discussed below.

Trace element variations

Trace element abundances in melt inclusions were obtained from crystals in seven clasts (Appendix C). For the Oruanui mineral assemblage, Rb and Ba are incompatible whereas Sr is compatible as it is incorporated into plagioclase. Figure 7 shows the variation of selected trace elements versus Rb. As shown in Fig. 7, most inclusions (80% of total) are confined to a limited range between 100 and 140 ppm Rb. However, several observations can be made:

1. The entire range of trace-element concentrations can be observed in inclusions from a single pumice clast, which is consistent with mixing in the crystal population. Trace-element contents in all melt inclusions vary by factors of 2.1–2.7 for compatible elements (e.g., 2.2 for Ti, 2.1 for Zr, and 2.7 for Sr) and by 1.5–4.4 for most incompatible trace elements (e.g. ~1.8 for Rb but ~11.0 for Pb).
2. Reentrants in quartz crystals from early- and late-erupted pumice clasts have similar trace element concentrations, implying that they equilibrated with the same host melt composition. All reentrant compositions are concentrated in a small range between 80 and 110 ppm Sr and 100 and 120 ppm Rb (exceeding 2σ counting errors, Fig. 7a) with the majority (~90%) containing >90 ppm Sr.
3. Most late-erupted melt inclusions follow a different trend from most early ones and show similar variations to the reentrants. In the Sr–Rb plot (Fig. 7a), the majority of late-erupted melt inclusions lie in the same region as reentrants (i.e., relatively high Sr and low Rb) whereas early melt inclusions are evenly spread across the whole range. Of the late melt inclusions 76% have >90 ppm Sr whereas only 32% of early melt inclusions have Sr > 90 ppm. In LREE–

Rb plots (e.g., La–Rb in Fig. 7c), five early-erupted melt inclusions, the majority of late-erupted melt inclusions (all but six), and all reentrants follow a steeper trend than the majority of early melt inclusions. These patterns are difficult to explain by, and unlikely to result solely from, crystallization processes.

4. Matrix glasses overlap with melt inclusions in the less differentiated end (low Rb and low Ba) of the variation plots of incompatible trace elements. These relations are again problematic for crystallization differentiation being the sole cause of the compositional diversity because, for example, ~33 wt% crystallization is necessary to increase Rb from 110 ppm in matrix glass to the highest value of 161 ppm in melt inclusions.
5. Multiple inclusions in several quartz grains were exposed and analyzed (Fig. 8, Appendix C). Melt inclusions in three crystals show increasing Sr from interior to near the rim, which is plausibly caused by addition of Sr to the system by magma mixing. Two crystals show decreasing Sr of melt inclusions from interior outward, which is consistent with crystallization. The increase of Sr contents from melt inclusions to reentrants is contrary to that expected for closed system crystallization differentiation and is plausibly the result of magma mixing. However, reaction between melt and Sr-rich country rocks is another possibility.
6. Despite the observations above which imply that some magma mixing must have occurred, the correlations between trace elements, especially in early-erupted melt inclusions, are consistent with crystal fractionation (see discussion below). The gap in Sr versus Rb plot (Fig. 7a) between pumice clasts and melt inclusions is a result of plagioclase in the pumice clasts as shown by the contrast between whole-pumice and glass compositions (Wilson et al. 2005). On a diagram of Sr/Rb versus Ba/Rb plotted on a logarithmic scale (Fig. 9), the slope of the trend defined by the data is in effect diagnostic of the relative roles of plagioclase and K-feldspar during crystallization, as we discuss below. A linear fit to ln(Ba/Rb) versus ln(Sr/Rb) of melt inclusions and reentrants gives a slope of 0.23 ± 0.01, which is the ratio of $(D_{Ba}-D_{Rb})/(D_{Sr}-D_{Rb})$, where D is the bulk distribution coefficient.

Composition of melt inclusions in jagged cores and surrounding dark zones (JC-MIs)

Of ~100 melt inclusions analyzed, six are located within the jagged CL cores and the surrounding dark CL regions (JC-MIs), four of which were analyzed for volatile contents. Dissolved H_2O concentrations in JC-MIs are indistinguishable from other melt inclusions, but CO_2 contents are at the low end of the whole range

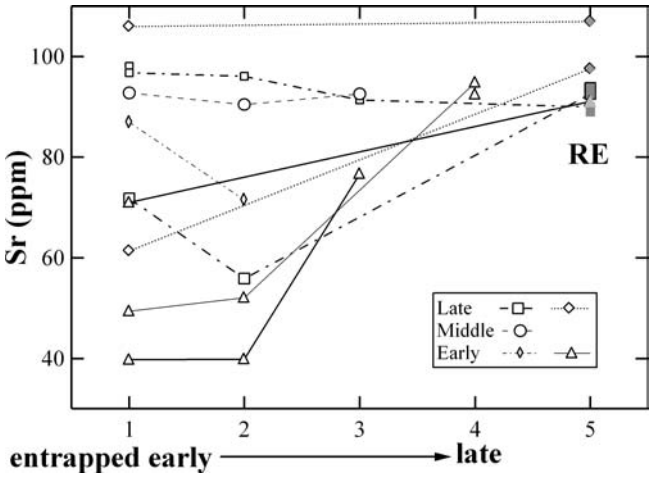

Fig. 8 Sr in different melt inclusions in single quartz grains. *Symbols* connected by lines are in the same crystal. *Open symbols* are melt inclusions and *filled ones* are reentrants. The number on the *x*-axis plots the relative position of melt inclusion on the 2-D wafer surface based on CL images. Inclusions in the interior formed earlier than those close to rim. When both inclusions are at similar distances from the crystal rim, their relative positions are determined by the CL zonation. Because of this qualitative determination on the relative entrapment time, it is meaningless to compare different grains

(Fig. 5a). Although scarce, JC-MIs vary widely in trace element concentration, from values similar to other melt inclusions to the lowest Ba and Sr, and highest Rb values found (symbols with plus signs in the center: Fig. 7). Most distinctively, JC-MIs define a negative trend in the Ba-Rb plot (Fig. 7b), which cannot be explained by crystallization of the Oruanui phenocryst assemblage or by mixing along the Oruanui pumice and melt inclusion trend (Fig. 9 and discussion below). The slope of a linear fit to ln(Ba/Rb) and ln(Sr/Rb) data of JC-MIs is $\sim 0.56 \pm 0.06$ (Fig. 9), which requires the involvement of minerals relatively rich in Ba (K-feldspar and/or biotite).

Discussion

Evolution of Oruanui rhyolite

Results from the CL zoning of quartz grains and trace element variations in melt inclusions show that incomplete assimilation/partial melting, crystallization differentiation, and magma mixing all occurred in the magma that was assembled to form Oruanui rhyolites. However, compositional variations are insufficient to distinguish the effects of crystallization and magma mixing. We discuss each process in detail below.

Incomplete assimilation/partial melting

The irregular, jagged CL boundaries of some quartz cores are interpreted to reflect melting event(s). The

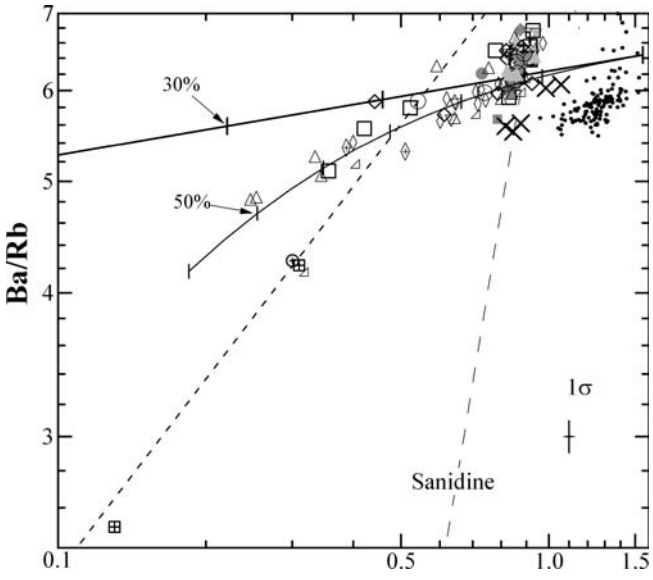

Fig. 9 Ba/Rb and Sr/Rb ratios of Oruanui samples. *Symbols* are the same as in Fig. 7. Fractional crystallization (*thick solid line*) or equilibrium crystallization (*thin solid curve*) of the Oruanui mineral assemblage can generate the observed variations of trace-element contents in melt inclusions. Bulk distribution coefficients for Rb, Sr and Ba are given in the caption of Fig. 7. The *long dashed line* labeled sanidine is the path for sanidine ($Ab_{34}Or_{65}$) using partition coefficients (D_{Rb} = 0.593 ± 0.008, D_{Sr} = 11.3 ± 0.7 and D_{Ba} = 28.4 ± 4.1) from Anderson et al. (2000). The *short dashed line* is fit to the data of JC-MIs. The 1σ uncertainty for ion-probe data is plotted and that for pumice and matrix glass (XRF data) is 0.025 for Sr/Rb and ~0.3 for Ba/Rb

cores themselves are thought to be residues of xenocrysts or antecrysts (crystals from solidified pre-intruded rocks, Charlier et al. 2005) rather than fragments of phenocrysts for the following reasons. First, the negative correlation of Ba versus Rb in JC-MIs (Fig. 7b) indicates that they formed in association with Ba-compatible minerals (plausibly K-feldspar). However, K-feldspar is absent from the < 320 ka eruptives at Taupo Volcano and very rare in TVZ rhyolites overall (Ewart 1966). The contrast between the inferred mineral assemblage for the JC-MIs and that of the Oruanui suggests that the jagged quartz cores are indeed xenocrystic. Second, the dark CL quartz zone surrounding the jagged CL core has lower Ti content than the bright CL quartz zone (Fig. 3), suggesting a different environment of formation (either a low formation temperature or a low activity of Ti in the melt, Wark and Watson 2004). Additional evidence for assimilation/melting comes from concurrent studies on Oruanui plagioclase grains (Charlier et al. 2003; in preparation) and Taupo zircon grains (Charlier et al. 2005). The zircon model ages in post-Oruanui rhyolites reported by Charlier et al. (2005) include some values similar to zircons in the Whakamaru ignimbrites (Brown and Fletcher 1999), which were erupted from a caldera that overlaps with the north Lake Taupo area (Wilson et al. 1986; Brown et al. 1998). It is interesting to note that the glass composition of Whakamaru type D pumice (analysis 1119 g in Table 2 in Brown et al. 1998) has a similar trace-element composition to one of the jagged core melt inclusion (Fig. 7).

Crystallization

Evidence of crystallization in the crystal population in Oruanui pumice clasts includes the normal zoning in plagioclase (Charlier et al. 2003), the euhedral morphology of crystals, and the oscillatory CL zoning inward from quartz crystal faces. Variations of trace elements in non-jagged-core melt inclusions, especially early-erupted inclusions, are generally consistent with crystallization (Fig. 7). At low degrees of crystallization, fractional and equilibrium crystallization generate similar trace-element contents except for compatible elements (Sr, Fig. 7). Compared to the calculated crystallization trends (fractional and equilibrium), the total variations in Sr, Rb and Ba of non-jagged-core melt inclusions can, to a first order, be equated to ~30 wt% for fractional crystallization and ~50 wt% for equilibrium crystallization (Fig. 7, 9). The estimate of total crystallization in the bulk magma, based on variations in pumice compositions, is ~28 wt% (Wilson et al. 2005). An important point is that all of the above values are much greater than 4–13 wt% of crystals in pumice clasts and some removal of crystals from the magma is needed.

Magma mixing

Other aspects of our data can best be explained by magma mixing. First, reentrant melt (now glass) and most late-erupted melt inclusions have similar trace element concentrations. If closed system evolution occurred, late-erupted melt inclusions and reentrants should differ in composition because residual (reentrant) melt would have suffered the most differentiation and have the most evolved composition (e.g., highest Rb and least Sr). This compositional similarity reflects one or more relatively late mixing events that caused crystallization of some late-erupted phenocrysts and late entrapment of some melt inclusions within them. Second, trace elements in multiple melt inclusions trapped in the same crystal vary unsystematically with apparent sequence of crystal growth and inclusion entrapment as shown in Fig. 8. This requires some unsteady compositional evolution of melt (the magma might change as a result of episodic magma mixing or crystals might move from one magmatic environment to another). Third, reentrants and most late-erupted melt inclusions form a different trend from early melt inclusions in the REE-Rb plot (e.g., La–Rb in Fig. 7c). To generate these different trends by crystallization, different mineral assemblages are required. However, the mineral assemblages are the same in early and late

erupted pumice clasts; the only variation is in the relative proportions of amphibole and orthopyroxene between the least- and most-evolved rhyolites (Wilson et al. 2005). The path of magmatic La and Rb differentiation is insensitive to variations in relative amounts of minor, mafic silicates. Thus the different La versus Rb trends reflect processes other than closed system crystallization differentiation.

Magma mixing shortly prior to eruption is also indicated by some features in pumice clasts, notably in the ranges of mineral compositions in single pumice clasts, and in the chemical and isotopic variations of the rhyolitic pumices (Wilson et al. 2005). If there were only two end members that mixed together, the arrays of compositions should be a straight line on any two element plot. This is not the case. Rather, after consideration of the analytical uncertainties, it would not be inconsistent to state that the data for Sr, Ba and Rb follow a single, but curved course (Fig. 7a, b). The petrographic features of the Ba-poor but Rb-rich melt being associated with jagged CL cores and Ba-rich minerals being absent point to the addition of Ba-poor melt as the plausible cause of the observed curved trend of compositional variations. However, a detailed model requires a better knowledge of the end-member compositions.

Pre-eruptive zonation of the Oruanui magma body

Wilson et al. (2005) report that the average composition of rhyolitic pumice clasts of each eruption phase is similar but that the ranges in compositions show some significant changes between eruption phases, notably in phase 3 when the vent location changed. These variations are interpreted to reflect some second-order geographic variations in magma composition. Even within the single clasts of evolved composition examined here, different records are preserved by pumices versus melt inclusions: the former records variations at the time of eruption, whereas melt inclusions preserve information on melt compositions that was obscured by a later mixing event. Early-erupted melt inclusions differ substantially in composition from most of late-erupted melt inclusions (Fig. 7): most late-erupted inclusions form a weak positive Sr–Rb correlation whereas early ones follow negative Sr–Rb trend, and most late inclusions form a steeper trend than early ones in the La–Rb plot. However, compositions of late-erupted melt inclusions are similar to reentrants. Therefore, early-erupted melt inclusions, and probably their host phenocrysts as well, may have formed in a different, and compositionally varied melt, and subsequently mixed into or possibly sank into the comparatively uniform reentrant melt. The compositional zonation in the Oruanui melt may have been transitory: melt plausibly evolved from a compositionally zoned or diverse body, to one with diminished variation, particularly of its melt.

Relation of gas and dissolved volatiles

Whether or not a magma is saturated with gas, we may compute, based on analyzed concentrations of H_2O and CO_2, a pressure at which the melt would be saturated with gas. In some cases this also requires an independent assessment of the temperature, because the solubilities of H_2O and CO_2 depend slightly on temperature. For high-silica rhyolite melts such as the Oruanui melt inclusions, which are near-eutectic compositions, the presence of phenocrysts (liquidus condition) assures a dependent relation between dissolved H_2O and CO_2 and temperature, as documented in experimental works (Holtz et al. 2001) and this provides a basis for estimating the equilibrium crystallization temperature. We term this computed pressure the gas-saturation pressure. The analyzed H_2O and CO_2 concentrations thus suffice to compute the gas-saturation pressure, and this pressure applies strictly to the volatile-bearing magma. Although, according to equilibrium, the magma cannot be at a pressure less than the gas-saturation pressure, it may be at a greater pressure, if the magma, in fact, lacks gas (is undersaturated with gas).

Remarkably, two closely related melts suffice also to determine the amount (mass fraction) of gas in the evolving magma. Several assumptions are required, however. First the magma must be gas-saturated. Second, the magma must be a closed system in either or both of two ways: (a) with crystallization neither gas nor crystals leave or join the magma; (b) no crystallization occurs and exsolving gas accumulates in the magma as it undergoes decompression and eruption. Third, it is necessary to know the amount of crystallization that occurred to cause the volatiles to exsolve and change the dissolved volatile concentrations. This can be assessed, following Wallace et al. (1995, 1999 and see Fig. 5b), by assuming fractional crystallization and measuring the change in concentration of non-volatile elements such as uranium (incompatible) and strontium (compatible in plagioclase). Special cases are those where we assume that no crystallization occurs, as done by Newman et al. (1988) in their study of crystal-poor obsidian. Two end-member special cases then result respectively for open system (gas loss) versus closed system (gas retention) decompression (shown on Fig. 5b). Fourth and finally, the dissolved concentrations of at least two gas species must be measured, and these must have substantially different solubilities, as happens to be the case for H_2O and CO_2.

The various possibilities are shown on Fig. 5b. Evolutionary paths for a magma with about 4.8 wt% of dissolved H_2O and 300 ppm of dissolved CO_2 are shown. If the pressure is larger than the gas-saturation pressure (about 190 MPa in the illustration) then closed system crystallization of volatile-free crystals causes the dissolved concentrations of H_2O and CO_2 to increase so that the ratio of H_2O to CO_2 remains constant (dashed line trending radially from the origin). Thus establishment by analysis that H_2O and CO_2 evolve in fixed

proportion to each other would suggest that the magma lacked gas (gas undersaturated).

The remaining four trends are for gas-saturated magma. The heavy line shows the changing concentrations of H_2O and CO_2 for isobaric conditions, and in this case the amount of gas initially present results in more or less change in dissolved H_2O and CO_2. For example if there were a very large excess of exsolved gas initially present, then this gas would buffer the concentrations of dissolved H_2O and CO_2 so that the concentrations change hardly at all as the magma crystallizes. Alternatively, if there were almost no excess gas at all initially, then the dissolved H_2O and CO_2 would change rapidly with crystallization and after only about 20 wt% of crystallization of the initial crystal-free magma the concentration of dissolved, incompatible H_2O would increase to about 5.8 wt% and the concentration of dissolved CO_2 would be vanishingly small (it would have been 'carried' into the gas by the much more abundant H_2O-rich gas). The preceding thought experiment helps inform the intuition regarding the necessary relations between relative solubilities, amounts of crystallization and amount of buffering gas.

The other three gas-saturated trends reveal the different effects of open (gas is lost as it exsolves) and closed (gas is retained) system degassing. Note that the trends for open and closed system degassing are nearly the same (practically indistinguishable), if there is negligible exsolved gas initially present. The other dotted curve for 10 wt% of exsolved gas initially present shows the effect of the large amount of initially exsolved CO_2 on buffering the concentration of dissolved CO_2.

Gas contents and bulk densities within the Oruanui magma body

Application of the above relations to natural magmas depends on the appropriate choice of circumstances based on petrography and volcanology. For the case of obsidian chips considered by Newman et al. (1988) crystallization can be assumed to be zero, leaving only the question of open versus closed system degassing with the possibility of some initial gas present for the closed system case. Evidently the magma could retain gas for the early part of its decompression and lose it later at low pressure; these complexities would cause scatter in the dissolved H_2O and CO_2 concentrations reflecting slightly different individual decompression and degassing histories of various parcels of magma. In the case of melt inclusions the concentrations of dissolved H_2O and CO_2 plausibly reflect various circumstances of melt entrapment at magmatic pressure before eruptive decompression. Melt inclusions close together in the same crystal likely formed as the crystal grew and closed off access to the surrounding melt, and such inclusions best justify the closed-system crystallization approach. If magma mixing accompanies crystallization, then we cannot assume a closed system, and it may not be possible to justify an estimate of the amount of exsolved gas present during the mixing and associated crystallization. Upon eruption, a different situation exists, whereby the magma decompresses so rapidly that further crystallization is negligible. In this case we may use reentrants, which provide samples of melt protected from significant vesiculation so that their concentrations of dissolved H_2O and CO_2 can be measured. We expect the melt in such reentrants initially to closely approach equilibrium with the surrounding gas. This is because initial decompression is slow as the magma is a viscous foam. But temperature is still high, the distance for diffusion is small (few tens of microns) and, of greatest importance, the gas is being retained in the foam. At lower pressure the foam becomes a spray (at the fragmentation pressure), which moves so rapidly that equilibrium can no longer be assumed between reentrant melt and escaping gas. All of the melt in a single clast has had the same decompression history, but the variable sizes and shapes of reentrants provide an array of partial decompressions that can reveal the amount of gas initially present. This is the main approach used in this work, so to avoid the potential effect of magma mixing. However, it will be of interest to compare estimates of gas content based on melt inclusions (some of which plausibly may have formed prior to magma mixing, possibly as closed systems) with those based on reentrants. After all, these should be similar, if the magma remained fairly closed as it crystallized—crystallization might occur after mixing for example.

Based on the correlations of early- and middle-reentrants to the trajectories of closed-system decompression (Fig. 6), we infer that the exsolved gas was ~0.3 wt% for early and ~0.5 wt% for middle melt at the beginning of magma ascent. As crystal contents in different pumice clasts are also similar, the early- to middle-erupted magmas would have had similar bulk densities at the time of eruption.

Dissolved H_2O and CO_2 contents in late reentrants cover a large range (Fig. 6a). All but two reentrants fall along the decompression trends with ~0.5–10 wt% gas. One reentrant (5.05 wt% H_2O and 10 ppm CO_2) seems to follow the closed-system crystallization trend with late melt inclusions. Another reentrant (2.14 wt% H_2O and 144 ppm CO_2) has a CO_2 content too high for decompression degassing and may be equilibrated with a CO_2-rich gas. We suggest that there is a possibility that some late-erupted magma contained high pre-eruptive gas contents. This is indeed not physically implausible for an unstable lower boundary layer, which possibly contained a lot of gas that might have been supplied from below, accompanying mafic recharge.

For comparison, we also estimated gas content using melt inclusions and the approach of Wallace et al. (1995, 1999). We calculated the mass fractions of crystallization implied by the observed ranges of Rb, Ba, and/or La, Th, and U (Table 3). Mass conservation equations show that the exsolved gas content at the time of crystallization was 0.9–5.4 wt% for early-erupted melt inclusions,

Table 3 Pre-eruptive gas contents (M_g) assuming closed-system fractional crystallization.[a]

	H_2O (wt%)	CO_2 (ppm)	P_{sat} (MPa)	M_w^{g} [b]	Rb (ppm)	Ba (ppm)	La (ppm)	Th (ppm)	U (ppm)	F[c] (wt%)	M_g (wt%)
Late											
P1541/T3-2-2-2	4.89	197	172	0.64	106	691	27.1	19.0	3.95		
P1541/T3-2-5-1	4.43	146	140	0.67	129	840	31.1	21.1	4.87	20 (7)	14.5 (3.0)
Middle											
P1508-1-4	4.53	136	143	0.69	120	716					
P1508-2-3-1	4.29	119	128	0.7	125	735				5	12.2 (0.6)
P1508-2-7-2	4.33	103	127	0.732	101	645					
P1508-2-1	4.47	83	130	0.781	109	670				9	1.4
Early											
P1412-2-26	4.91	101	155	0.776	117	690	23.5	16.6	3.8		
P1412-2-23-2	5.07	80	159	0.82	153	828	27.2	21.7	4.7	24 (4)	5.4 (1.0)
P1412-2-25	4.50	136	141	0.69	109	642	23.2	17.1	3.4		
P1412-2-23-2	5.07	80	159	0.82	153	828	27.2	21.7	4.7	28 (7)	2.1 (0.8)
P1573-1-5-1	4.84	34	139	0.908	117	735	26.5	18.6	4.2		
P1573-1-7-i2	4.45	27	119	0.915	148	777	32.0	28.4	6.2	25 (10)	17 (4.0)
P1573-1-2-1	4.28	80	120	0.773	107	650	23.1	14.2	2.9		
P1573-1-7-i2	4.45	27	119	0.915	148	777	32.0	28.4	6.2	40 (12)	2.6 (0.8)
P1573-1-3	4.34	76	122.7	0.787	100	616	23.1	14.8	3.3		
P1573-1-5-1	4.84	34	139	0.908	117	735	26.5	18.6	4.2	21 (5)	0.9 (0.5)
P1573-2-3	4.64	106	142	0.75	115	682	24.7	15.2	3.5		
P1573-1-7-1	4.85	59	144	0.85	152	767	25.0	16.9	3.6	12 (10)	0.9 (1.1)
P1573-1-2-2	4.53	123	140.2	0.713	119	677	24.3				
P1573-1-7-1	4.85	59	144	0.852	152	767	25.0			16 (10)	0.9 (1.0)

[a] Pre-eruptive gas contents for closed-system gas-saturated fractional crystallization were calculated using the approach of Wallace et al. (1995). Pairs of melt inclusions with similar P_{sat}, decreasing CO_2 and Sr, and increasing incompatible trace elements (Rb, Ba, La) were chosen from each clast. Each pair of inclusions can yield one value of M_g (fraction of gas in wt%). For some pairs, the estimated F is larger than the observed crystal content. Therefore, the assumption of a closed-system is only approximate

[b] M_w^{g} is the mass fraction of water vapor in gas that is equilibrating with the H_2O in the melt, which is calculated using the solubility model of Liu et al. (2005)

[c] F is the crystallization amount (wt%) obtained by averaging values calculated using $\ln(1\text{-}F)=\ln(C_A/C_{A,\,0})/(D^A-1)$ for selected trace elements (Rb, Ba, La, and/or Th, U). Bulk distribution coefficients for Rb (0.07), Ba (0.47), La (0.32), Th (0.04), and U (0.05) are estimated using the Oruanui phenocryst assemblage (72 wt% plagioclase, 10 wt% quartz and orthopyroxene, and 2 wt% amphibole). Distribution coefficients of Rb, Ba, La for plagioclase and La for orthopyroxene are from Nash and Crecraft (1985), those of Rb and Ba for orthopyroxene and amphibole are from Ewart and Griffin (1994), and those of La for amphibole and U and Th for all minerals are from the GERM database (http://earthref.org/GERM).

~12.2 wt% for one pair of middle-erupted melt inclusions, and ~14.5 wt% for one pair of late-erupted melt inclusions (Table 3). These values are substantially larger than the estimates from reentrants, and this disparity may reflect some combination of magma mixing and bubble accumulation.

Conclusions

The evolution of the Oruanui magma body is shown by quartz-hosted melt inclusion compositions to have involved complex combinations of partial assimilation/melting of pre-existing plutonic rocks, crystallization differentiation, magma mixing, and gas saturation. CL images of Oruanui quartz crystals reveal the presence of minor amounts of jagged cores, which were derived by partial assimilation/melting of a source that included a Ba-compatible mineralogy, plausibly plutonic rocks associated with earlier Whakamaru ignimbrite magmatism in the Taupo area. Trace-element variations of all melt inclusions and reentrants in the non-jagged-core regions are consistent with the effects of assimilation, crystallization and magma mixing. However, because of the small range of trace-element variations and uncertainties in partition coefficients, it is difficult to distinguish which differentiation mechanism is dominant. Multiple melt inclusions and reentrants in single quartz crystals show that magma mixing probably occurred multiple times. However, the complex CL zoning pattern of Oruanui quartz requires a more detailed study on the multiple melt inclusions in individual quartz crystals.

Overall abundances of dissolved H_2O and CO_2 in melt inclusions and reentrants in the non-jagged-core regions are consistent with gas-saturated conditions during evolution of the Oruanui magma body. Based on saturation pressures of H_2O and CO_2, the depth of the top of the Oruanui magma body was ~3.5 km below the surface and the vertical thickness of magma tapped during the eruption was ~3.5 km, consistent with independent estimates of magma volume (~530 km^3) divided by the area of the structural caldera (140 km^2). Based on variation of H_2O and CO_2 contents in reentrants, the Oruanui magma body contained increasing amount of exsolved gas with depth. This increasing gas content would have caused decreasing density of the magma with depth, plausibly leading to convective instability and mixing. Studies of dissolved volatile

contents in reentrants in crystals from the late erupted portions of other pyroclastic rhyolites would indicate whether such mixing events are common, particularly for rhyolites like the Bishop Tuff which otherwise show clear systematic gradients in composition.

Acknowledgements This work was supported by US NSF grants EAR 0106327 and 0408707, Marsden Fund grant GNS 202 from the Royal Society of New Zealand, and the New Zealand Foundation for Research, Science & Technology. Thorough and thoughtful reviews by Tom Vogel, Tim Grove, and Charlie Bacon are appreciated. We also thank Youxue Zhang for his generosity in allowing us access to the FTIR spectrometer at the University of Michigan.

References

Anderson AT (1991) Hourglass inclusions—theory and application to the Bishop rhyolitic Tuff. Am Mineral 76:530–547

Anderson AT, Davis AM, Lu FQ (2000) Evolution of Bishop Tuff rhyolitic magma based on melt and magnetite inclusions and zoned phenocrysts. J Petrol 41:449–473

Arculus RJ, Belfield S-J, Earl KL (2005) Tracking development of the Taupo (New Zealand) rhyolitic magma chamber through melt inclusions. EOS Trans AGU 86(18), Jt Assem Suppl, Abstract V22A-03

Bacon CR (1989) Crystallization of accessory phases in magmas by local saturation adjacent to phenocrysts. Geochim Cosmochim Acta 53: 1055–1066

Behrens H, Tamic N, Holtz F (2004) Determination of molar absorption coefficient for the IR absorption band of CO_2 in rhyolitic glasses. Am Mineral 89:301–306

Brown SJA, Fletcher IR (1999) SHRIMP U-Th dating of the preeruption growth history of zircons from the 340 ka Whakamaru Ignimbrite, New Zealand:evidence for >250 k.y. magma residence times. Geology 27: 1035–1038

Brown SJA, Wilson CJN, Cole JW, Wooden J (1998) The Whakamaru group ignimbrites, Taupo Volcanic Zone, New Zealand: evidence for reverse tapping of a zoned silicic magmatic system. J Volcanol Geotherm Res 84: 1–37

Charlier BLA, Davidson JP, Wilson CJN (2003) Generation processes in a high-silica rhyolite as recorded in plagioclase crystals from Taupo volcano, New Zealand. Geochim Cosmochim Acta 66(Suppl 15A):130

Charlier BLA, Wilson CJN, Lowenstern JB, Blake S, van Calsteren PW, Davidson JP (2005) Magma generation at a large, hyperactive silicic volcano (Taupo, New Zealand) revealed by U-Th and U-Pb systematics in zircons. J Petrol 46:3–32

Davy BW, Caldwell TG (1998) Gravity, magnetic and seismic surveys of the caldera complex, Lake Taupo, North Island, New Zealand. J Volcanol Geotherm Res 81:69–89

Dunbar NW, Hervig RL, Kyle PR (1989) Determination of preeruptive H_2O, F and Cl contents of silicic magmas using melt inclusions: examples from Taupo volcanic center, New Zealand. Bull Volcanol 51: 177–184

Ewart A (1966) Review of mineralogy and chemistry of the acidic volcanic rocks of Taupo Volcanic Zone, New Zealand. Bull Volcanol 29:147–172

Ewart A, Griffin WL (1994) Application of proton microprobe data to trace element partitioning in volcanic rocks. Chem Geol 117:251–284

Götze J, Plötze M, Habermann D (2001) Origin, spectral characteristics and practical applications of the cathodoluminescence (CL) of quartz—a review. Mineral Petrol 71:225–250

Hervig RL, Dunbar N, Westrich HR, Kyle PR (1989) Pre-eruptive water-content of rhyolitic magmas as determined by ion microprobe analyses of melt inclusions in phenocrysts. J Volcanol Geotherm Res 36: 293–302

Hildreth W (1977) The magma chamber of the Bishop Tuff: gradients in temperature, pressure and composition. PhD Dissertation, University of California, Berkeley, 328 pp

Hildreth W (1979) The Bishop Tuff: Evidence for the origin of compositional zonation in silicic magma chambers. Geol Soc Am Spec Pap 180:43–75

Hildreth W (1981) Gradients in silicic magma chambers: implications for lithospheric magmatism. J Geophys Res 86:10153–10192

Holtz F, Johannes W, Tamic N, Behrens H (2001) Maximum and minimum water contents of granitic melts generated in the crust: a reevaluation and implications. Lithos 56:1–14

Liu Y, Zhang Y, Behrens H (2005) Solubility of H_2O in rhyolitic melts at low pressures and a new empirical model for mixed H_2O–CO_2 solubility in rhyolitic melts. J Volcanol Geotherm Res 143:219–235

Lu FQ, Anderson AT, Davis AM (1995) Diffusional gradients at the crystal/melt interface and their effect on the composition of melt inclusions. J Geol 103:591–597

MacPherson GJ, Davis AM (1994) Refractory inclusions in the prototypical CM chondrite, Mighei. Geochim Cosmochim Acta 58:5599–5625

Nash WP, Crecraft HR (1985) Partition coefficients for trace-elements in silicic magmas. Geochim Cosmochim Acta 49:2309–2322

Newman S, Epstein S, Stolper EM (1988) Water, carbon dioxide, and hydrogen isotopes in glasses from the ca 1340 AD eruption of the Mono Craters, California: constraints on degassing phenomena and initial volatile content. J Volcanol Geotherm Res 35:75–96

Peppard BT, Steele IM, Davis AM, Wallace PJ, Anderson AT (2001) Zoned quartz phenocrysts from the rhyolitic Bishop Tuff. Am Mineral 86: 1034–1052

Skirius CM, Peterson JW, Anderson AT (1990) Homogenizing rhyolitic glass inclusions from the Bishop Tuff. Am Mineral 75:1381–1398

Smith RL (1979) Ash-flow magmatism. Geol Soc Am Spec Pap 180:5–27

Smith RL, Bailey RA (1966) The Bandelier Tuff; a study of ash-flow eruption cycles from zoned magma chambers. Bull Volcanol 29:83–103

Sutton AN, Blake S, Wilson CJN (1995) An outline geochemistry of rhyolite eruptives from Taupo Volcanic Center, New Zealand. J Volcanol Geotherm Res 68:153–175

Sutton AN, Blake S, Wilson CJN, Charlier BLA (2000) Late Quaternary evolution of a hyperactive rhyolite magmatic system: Taupo volcanic centre, New Zealand. J Geol Soc Lond 157:537–552

Wallace PJ, Anderson AT, Davis AM (1995) Quantification of pre-eruptive exsolved gas contents in silicic magmas. Nature 377:612–616

Wallace PJ, Anderson AT, Davis AM (1999) Gradients in H_2O, CO_2, and exsolved gas in a large-volume silicic magma system: interpreting the record preserved in melt inclusions from the bishop tuff. J Geophys Res 104:20097–20122

Wark DA, Watson EB (2004) The TITANiQ: a titanium-in-quartz thermometer. Geochim Cosmochim Acta 68 (Suppl):A543

Wilson CJN (1993) Stratigraphy, chronology, styles and dynamics of Late Quaternary eruptions from Taupo volcano, New Zealand. Phil Trans R Soc Lond A 343:205–306

Wilson CJN (2001) The 26.5 ka Oruanui eruption, New Zealand: an introduction and overview. J Volcanol Geotherm Res 112:133–174

Wilson CJN, Houghton BF, Lloyd EF (1986) Volcanic history and evolution of the Maroa-Taupo area, central North Island. In: Smith IEM (ed) Late Cenozoic volcanism in New Zealand. Royal Society of New Zealand Bulletin 23:194–223

Wilson CJN, Charlier BLA, Blake S, Sutton AN (2002) Pyroclastic deposits from ca 64 to 26.5 ka in the Maroa-Taupo area, New Zealand, reflect contemporaneous independent silicic magmatic systems. Eos, Trans Am Geophys Un 82 (22 suppl):Abstract SE 51B-01

Wilson CJN, Blake S, Charlier BLA, Sutton AN (2005) The 26.5 ka Oruanui eruption, Taupo volcano, New Zealand: development, characteristics and evacuation of a large rhyolitic magma body. J Petrol (in press)

Zhang YX, Behrens H (2000) H_2O diffusion in rhyolitic melts and glasses. Chem Geol 169:243–262

Zhang YX, Belcher R, Ihinger PD, Wang LP, Xu ZJ, Newman S (1997) New calibration of infrared measurement of dissolved water in rhyolitic glasses. Geochim Cosmochim Acta 61:3089–3100